Supplementary Information (SI) for Catalysis Science & Technology.
This journal is © The Royal Society of Chemistry 2026

Supporting Information

Synergistic Photocatalytic Production of H_2O_2 and Imines via Oxygen-Enriched Acetonitrile Medium and Benzylamine Oxidation

Xin Xu[a], Yuming Dong*[a] Yingxin Guo[a], Xinxin Jiang[a], Lizi Liu[a], Tingyu Yang[a], Xinyu Sun[a], Pengken Li[a], Hui Zhao[a], Yongfa Zhu[b] and Junshan Li[c]

a International Joint Research Center for Photoresponsive Molecules and Materials, Key Laboratory of Synthetic and Biological Colloids, School of Chemical and Material Engineering, Jiangnan University, Wuxi 214122, China

E-mail: dongym@jiangnan.edu.cn

b Department of Chemistry, Tsinghua University, Beijing 100084, China

c Institute for Advanced Study, Chengdu University, Chengdu 610106, China

Contents

1 Experimental Procedures

1.1 Experimental material

Benzylamine (BA) and N-Benzylidenebenzylamine (N-BA) were purchased from were purchased from Sinopharm Chemical Reagent Co. Ltd. And 3,4,9,10-perylenetetracarboxylic dianhydride (PTCDA), polyvinylpyrrolidone (PVP), N,N-Dimethylformamide (DMF), glycol, ethanol and other experimental reagents were purchased from Sinopharm Chemical Reagent Co., Ltd. All of the reagents were analytical grade without further purification. Deionized water was used throughout this study.

1.2 Details of the photocatalysis experiment

For all photocatalytic measurements (including rate and cyclic tests), we utilized a 300 W Xe lamp as the simulated sunlight source. To ensure consistent and uniform irradiation across all experiments, the reactor was always placed at the same fixed distance and orientation relative to the light source. The measured light intensity at the sample position was 325 Mw cm^{-1}.

1.3 Oxidation experiment of NBT

In a typical run, 8 mg prepared catalyst was suspended in 100 mL of NBT aqueous solution with a concentration of 2.0×10^{-5} M. The light source was a 300 W Xenon lamp (equipped with a λ>420 nm filter). Before irradiation, the suspension was continuously stirred in the dark for 30 min. After the reaction, 3 mL of reaction suspension was sampled. The photocatalyst was separated by centrifugation, and then the absorbance of supernatant was recorded on the UV-Vis spectrophotometer (UV-752, Shanghai Jinghua Technology Co., China). The photocatalytic generation of $\cdot O_2^-$ was determined by the degradation of NBT, which was monitored by the absorbance change at the wavelength of 259 nm

The superoxide radical produced was calculated according to the following formula:

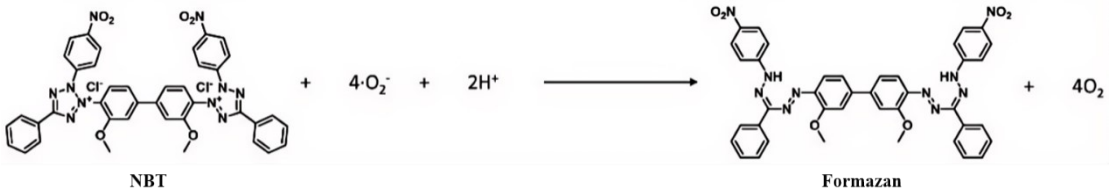

1.4 Calculation of Evaporation Energy Consumption

The formula for calculating the energy consumption of evaporation of acetonitrile and water is as follows:

$Q = Q_1 + Q_2 + Q_3 + Q_4$

$Q_{sensible} = m \times C_p \times \Delta T$

$Q_{latent} = m \times \Delta H_{vap}$

m: the quality of the solvent (kg)

C_p: the constant-pressure specific heat capacity of the solvent (J/kg·°C)

ΔT: temperature variation (°C)

ΔH_{vap}: the latent heat of vaporization of the solvent

Where Q1, Q2, Q3 and Q4 represent the heating energy consumption, energy consumption of vacuum pump, Cooling system energy consumption, and heat loss.

1.5 Experiment of RDE

Rotating disk electrode (RDE) measurements were performed using a CHI660D electrochemical workstation (Shanghai Chenhua Instrument Co., Ltd.) with a three-electrode system. The working electrode was a glassy carbon RDE (3 mm diameter) coated with the catalyst, a platinum wire served as the counter electrode, and an Ag/AgCl (saturated KCl) electrode was used as the reference. All measurements were conducted in an O_2 saturated phosphate buffer solution aqueous solution at room temperature. Linear sweep voltammetry (LSV) was recorded at rotation speeds of 400, 800, 1200, 1600, and 2000 rpm with a scan rate of 10 $mV \cdot s^{-1}$. The Koutecky-Levich (K-L) plots were analyzed using the following equation:

$$\frac{1}{I} = \frac{1}{I_L} + \frac{1}{I_K} = \frac{1}{B\omega^{1/2}} + \frac{1}{I_K}$$

where I is the measured current density, IL is the diffusion-limited current density, IK is the kinetic current density, ω is the angular rotation rate, and B is the Levich constant. The electron transfer number (n) was calculated from the slope of the K-L plots using the Levich equation:

$$B = 0.62nFD_{O_2}^{2/3}v^{-1/6}C_{O_2}$$

2 Results and Discussion

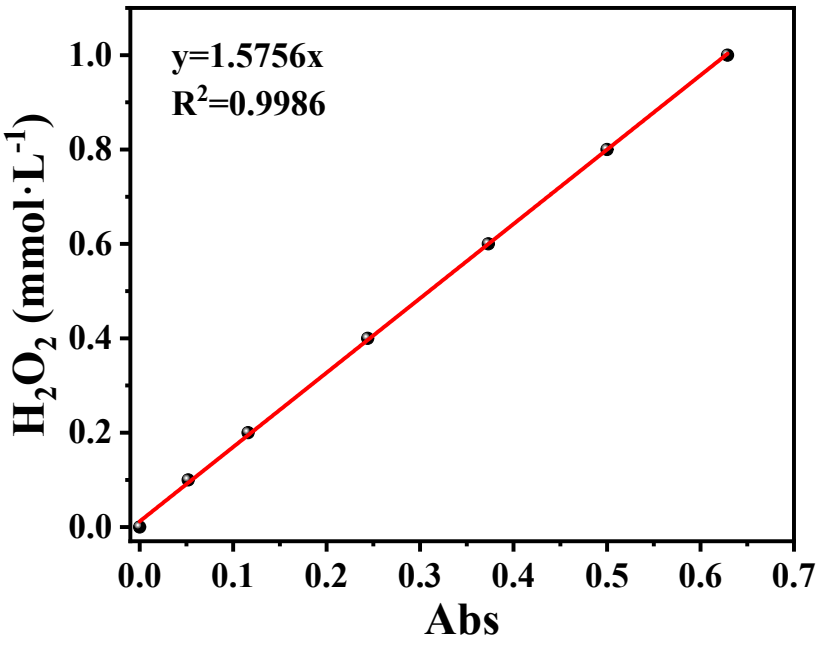

Figure S1. Standard curve of H_2O_2 concentration.

The final linear standard curve fitted was $y = 1.5756x$, where y is the concentration of H_2O_2 (mmol/L) and x is the absorbance, and the variance was 0.9986, which proved that the curve was fitted accurately and could be used to calculate the concentration of H_2O_2.

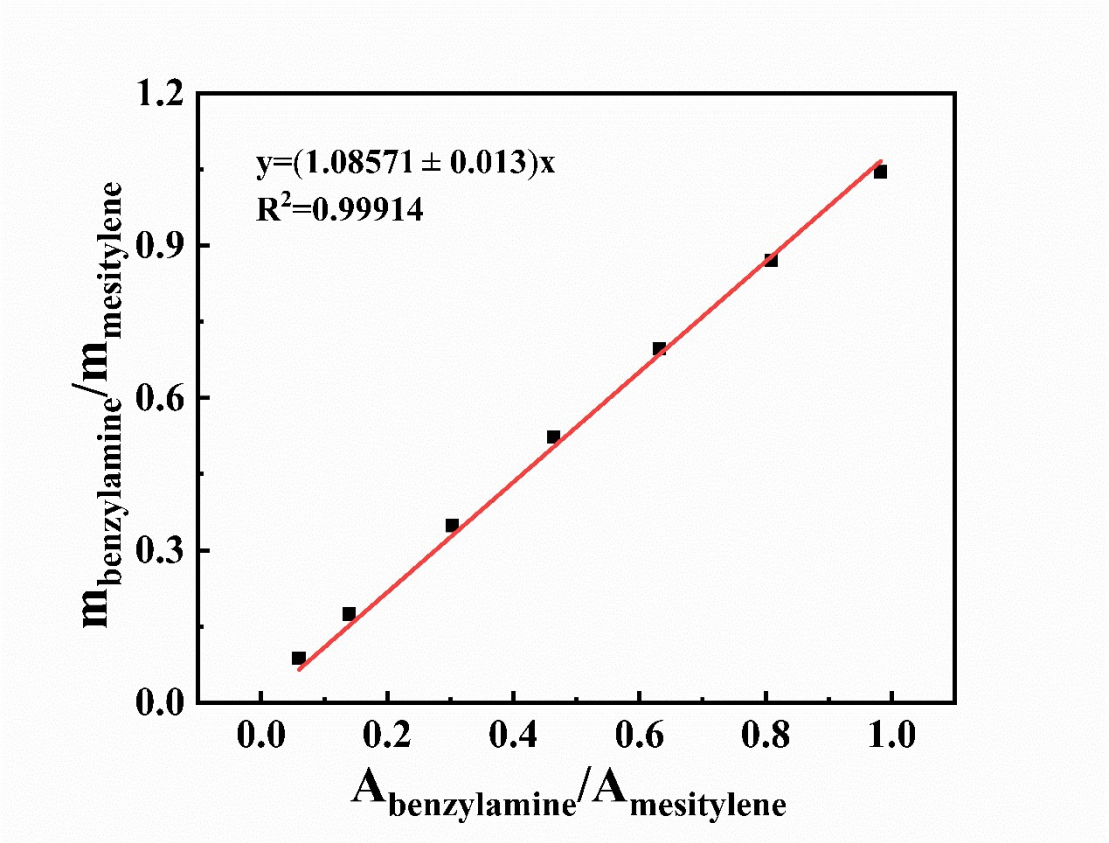

Figure S2. Standard curve of benzylamine.

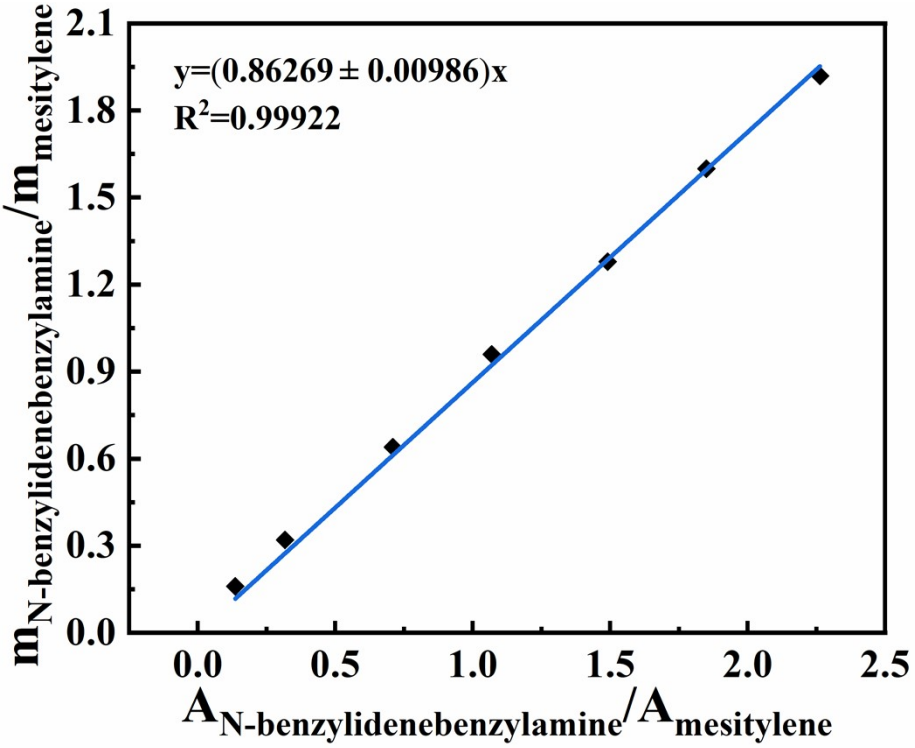

Figure S3. Standard curve of N-benzylidenebenzylamine.

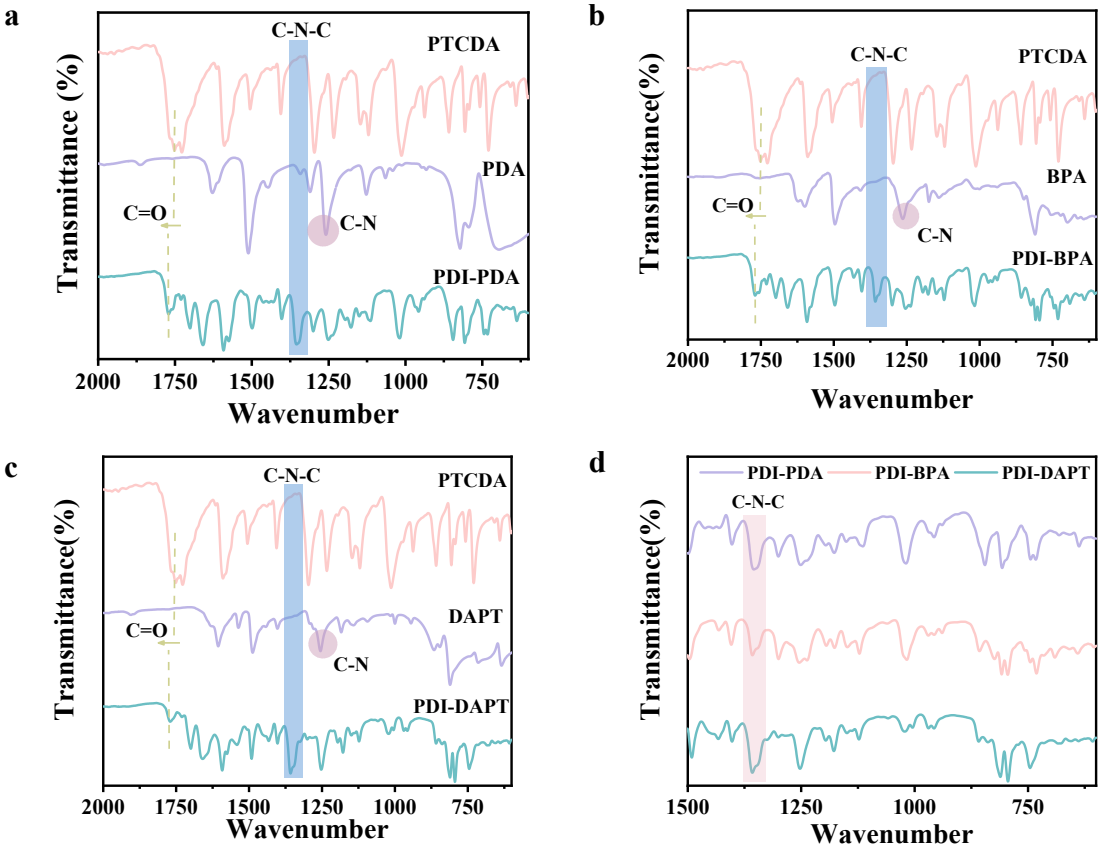

Figure S4. The Fourier transform infrared (FT-IR) spectra of high crystallinity linear conjugative polymers and their synthesis raw materials: (a) FT-IR of PTCDA, PDA and PDI-PDA; (b) FT-IR of PTCDA, BPA and PDI-BPA; (c) FT-IR of PTCDA, DAPT and PDI-DAPT; (d) FTIR spectra of PDI-PDA, PDI-BPA and PDI-DAPT.

As depicted in **Figure S4b**, The characteristic vibration peak of the C=O bond in PDI-PDA appears at 1777.84 cm^{-1} , which shows a significant shift compared to the vibration peak of the C=O bond in PTCDA anhydride (1749.45 cm^{-1})[1]. The intensity of the C-N stretching vibration peak near 1250 cm^{-1} of the PDA decreases, but a characteristic C-N-C peak appears at 1354.9 cm^{-1} . Fourier transform infrared (FT-IR) spectroscopy revealed a characteristic C=O stretching vibration at 1777.84 cm^{-1} in PDI-PDA, which is notably shifted from that of pristine PTCDA (1749.45 cm^{-1})[2]. Similarly, as depicted in **Figure S4a and c**, the synthesis of PDI-PDA and PDI-DAPT was accomplished through Imidazole solvent method.

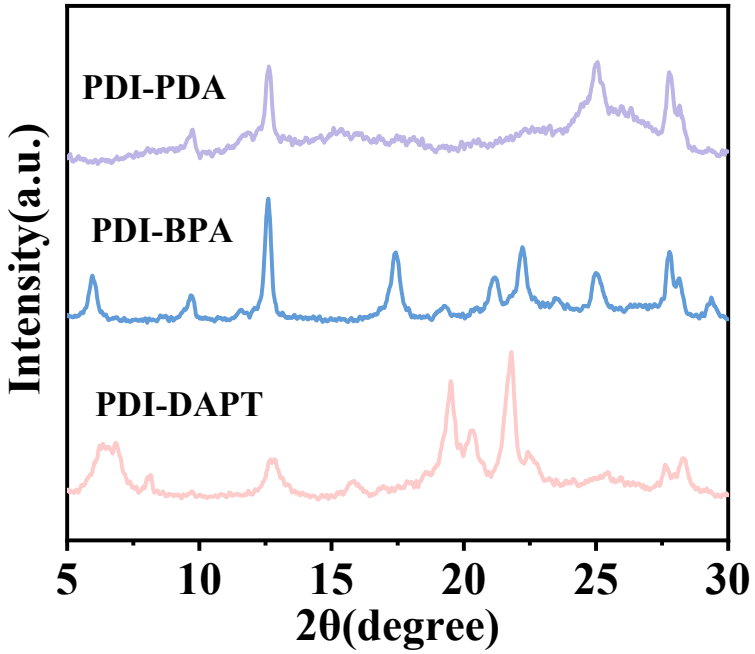

Figure S5. XRD patterns of PDI-PDA, PDI-BPA and PDI-DAPT

The crystallinities of the two samples were investigated by X-ray diffraction (XRD) patterns, The diffraction peaks of PDI-BPA are sharper and exhibit higher intensity compared to PDI-PDA and PDI-DAPT, indicating that PDI-BPA possesses higher crystallinity with more regular molecular arrangement, thereby demonstrating superior carrier mobility.

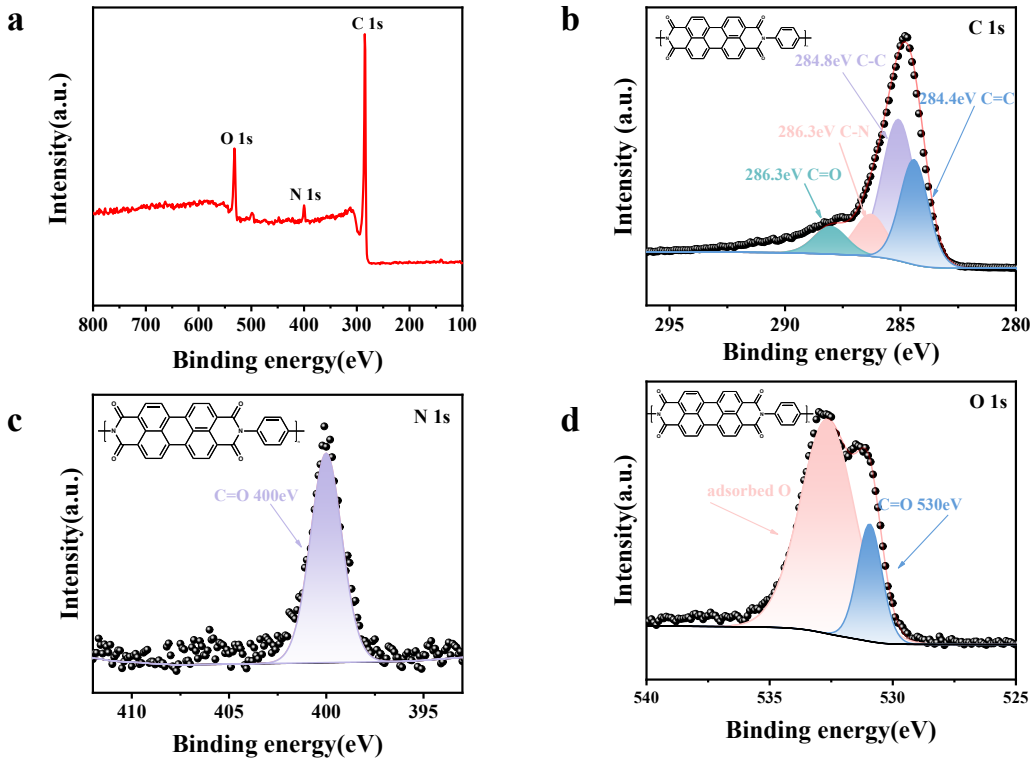

Figure S6. High resolution XPS of (a) C 1s, (b) N 1s and (c) O 1s in PDI-PDA; (a) X-ray photoelectron spectra (XPS) of PDI-PDA.

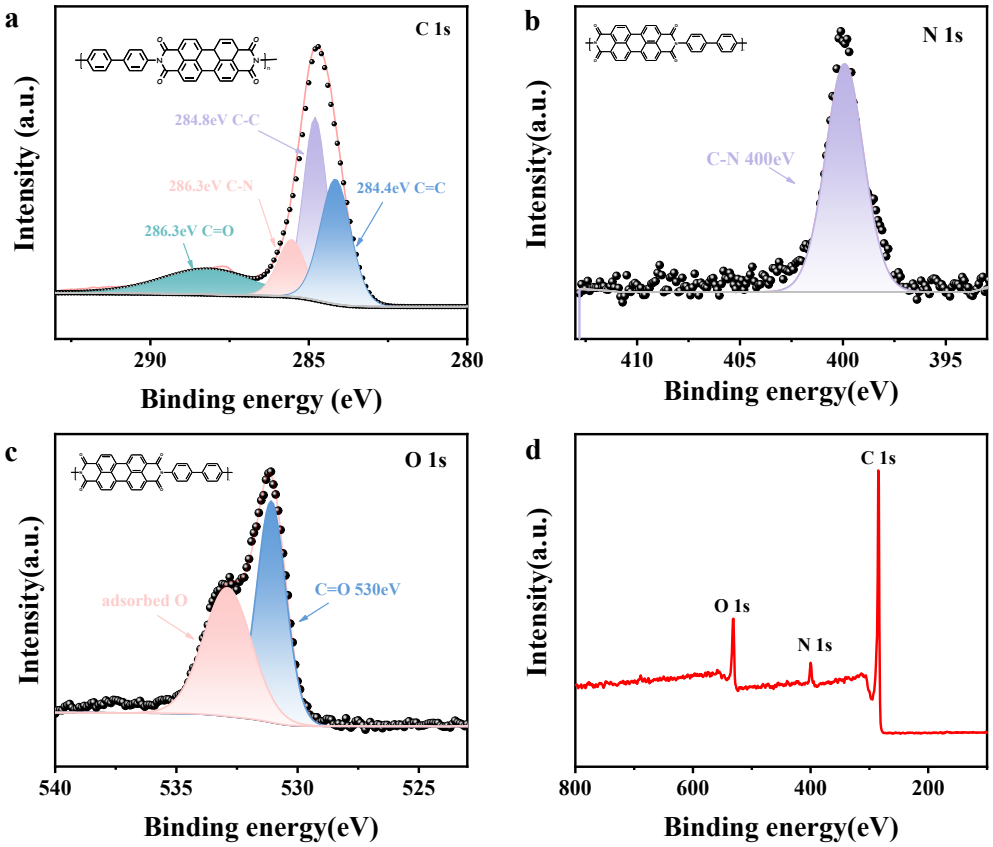

Figure S7. High resolution XPS of (a) C 1s, (b) N 1s and (c) O 1s in PDI-BPA; (a) X-ray photoelectron spectra (XPS) of PDI-BPA.

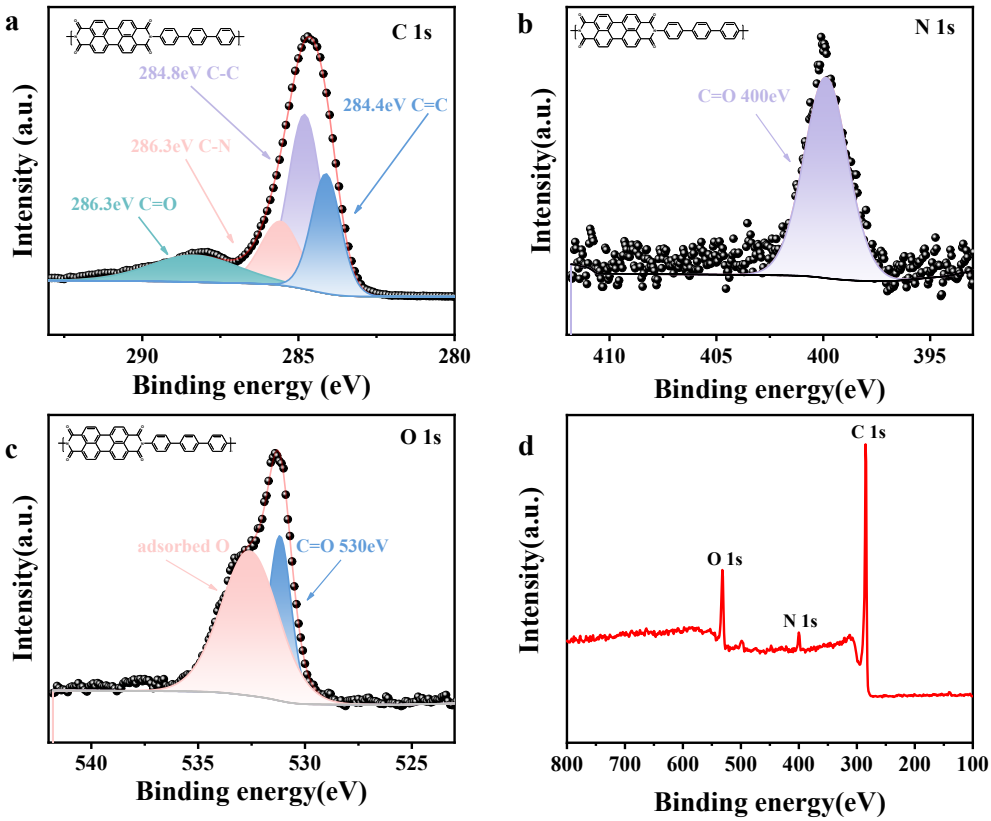

Figure S8. High resolution XPS of (a) C 1s, (b) N 1s and (c) O 1s in PDI-DAPT; (a) X-ray photoelectron spectra (XPS) of PDI-DAPT.

The X-ray photoelectron spectra (XPS) of PDI-BPA exhibits three types of signals: C 1s, N 1s and O 1s **(Figure S7d)**, which are consistent with its chemical composition. The four main peaks in the high-resolution C 1s XPS spectra of PDI-BPA can be attributed to C-C, C-N, C=C and C-O, respectively (**Figure S7a**)[3]. The signal peaks in the high-resolution N 1s XPS spectra of PDI-BPA can be corresponded to C-N (Figure S7**b**)[4]. The high-resolution O 1s XPS spectra of BAD was deconvoluted to form two main peaks, with the signal peak at 533.6 eV originating from C-O-C, while the other signal peak at 530.0 eV was believed to be formed by adsorbed O_2 (Figure S7**c**)[5]. Similarly, the XPS spectra of PDI-PDA and PDI-DAPT also confirmed their successful synthesis (Figure S6 **and** Figure **S8**).

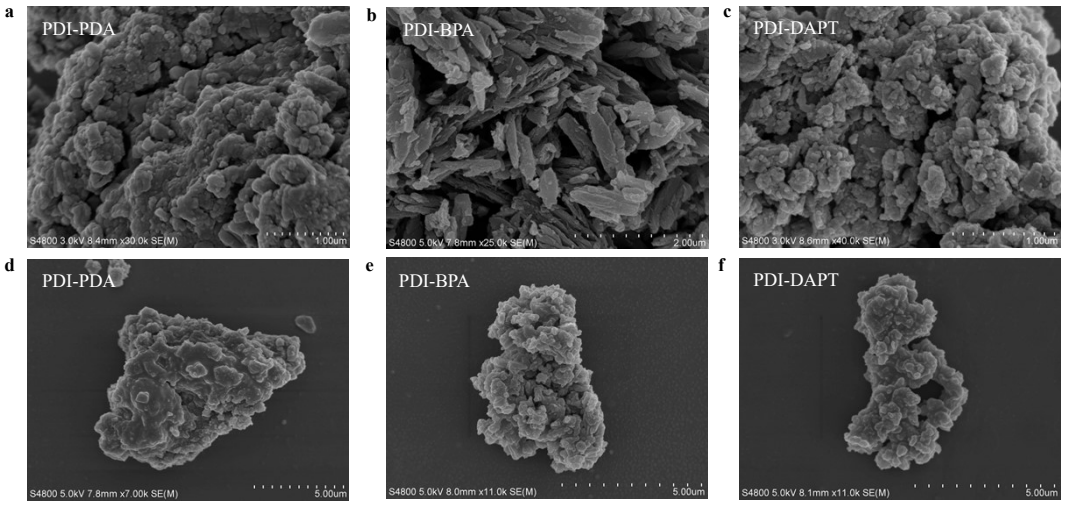

Figure S9. Field emission scanning electron microscopy (SEM) images of PDI-PDA, PDI-BPA and PDI-DAPT.

The SEM results of three high-crystallinity linear conjugated polymers are shown in **Figure S9.** All three photocatalysts are composed of stacked nanoscale crystalline polymers. Irregular sheet-like polymers were observed to interweave and stack on the surfaces of PDI-BPA, while PDI-PDA and PDI-DAPT was almost absent. These differences could be regarded as the result that linear conjugated polymers tend to π–π stacking.

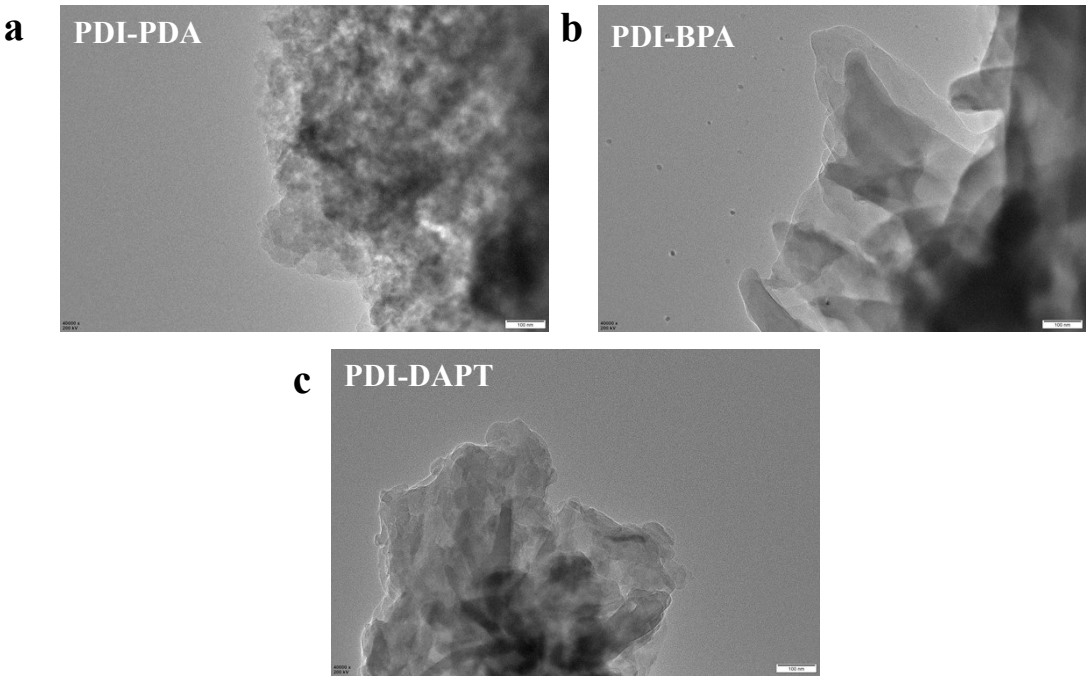

Figure S10. TEM images of (a) PDI-PDA, (b) PDI-BPA, and (c) PDI-DAPT.

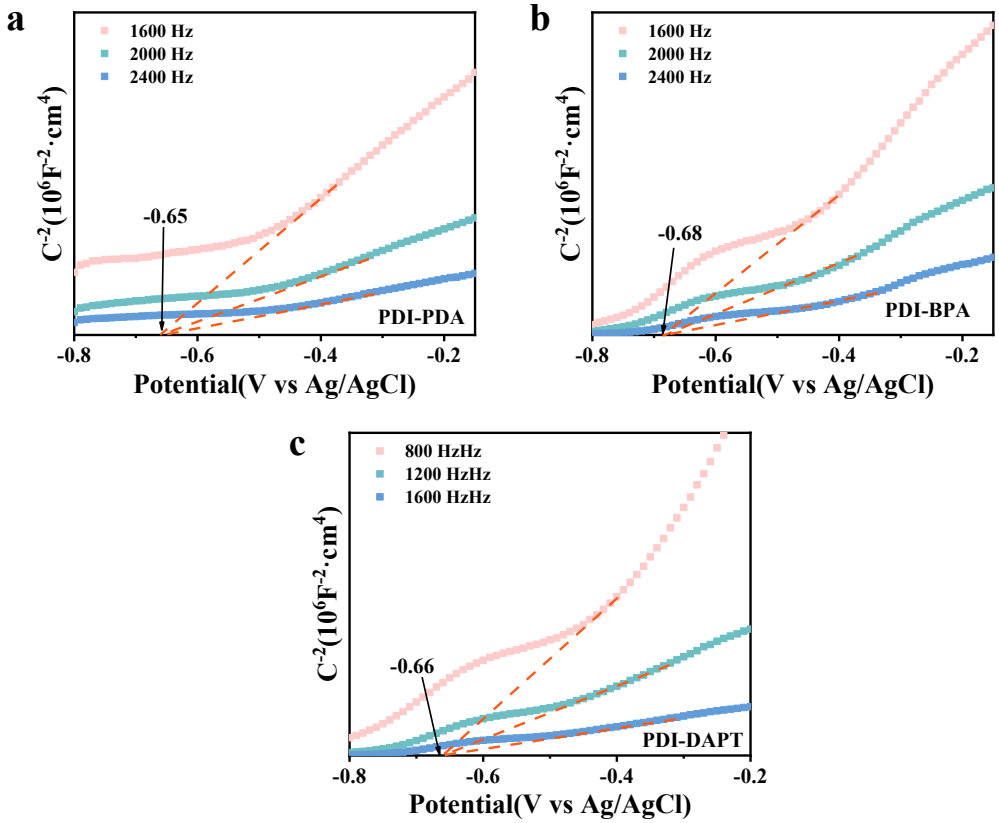

Figure S11. Mott-Schottky plots of (a) PDI-PDA, (b) PDI-BPA and (c) PDI-DAPT samples.

The edge position of the catalysts can be determined by electrochemical Mott-Schottky method. It can be seen from the results of **Figure S11** that the slope of the Mott-Schottky curves of the three photocatalysts is positive, indicating that they are all N-type semiconductors. The tangent intersection of the curve in **Figure S11** represents the flat band (FB) potential of each photocatalyst, and the corresponding conduction band (CB) position can be obtained through flat band potential conversion. The calculation formula is shown in **Equation 1**:

$$E_{CB}(V\ vs.\ NHE) = E_{FB}(V\ vs.\ AgCl/Ag) + 0.197 - 0.2 \quad (1)$$

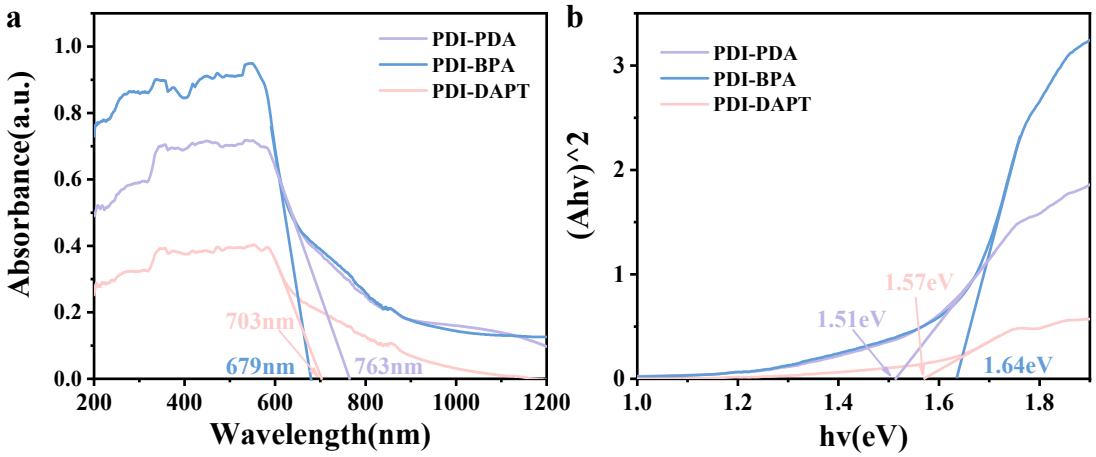

Figure S12. (a) UV-vis DR spectra of synthesized photocatalysts, (b). the Tauc plots.

The comparison among UV-vis DR spectra of PDI-PDA, and PDI-BPA and PDI-DAPT showed that the absorption peaks of the both are almost identical, and the intensities of the PDI-BPA catalyst are higher than those of the corresponding bands of PDI-PDA and PDI-DAPT. the Tauc plots (**Figure S12b**) determined the band gap of PDI-PDA, PDI-BPA and PDI-DAPT being 1.51, 1.64 and 1.57 eV.

If the conduction potential (E_{CB}) and band gap (E_g) are known, the conduction potential (E_{VB}) can be calculated by **Equation 2**:

$$E_{VB} = E_{CB} + E_g \quad (2)$$

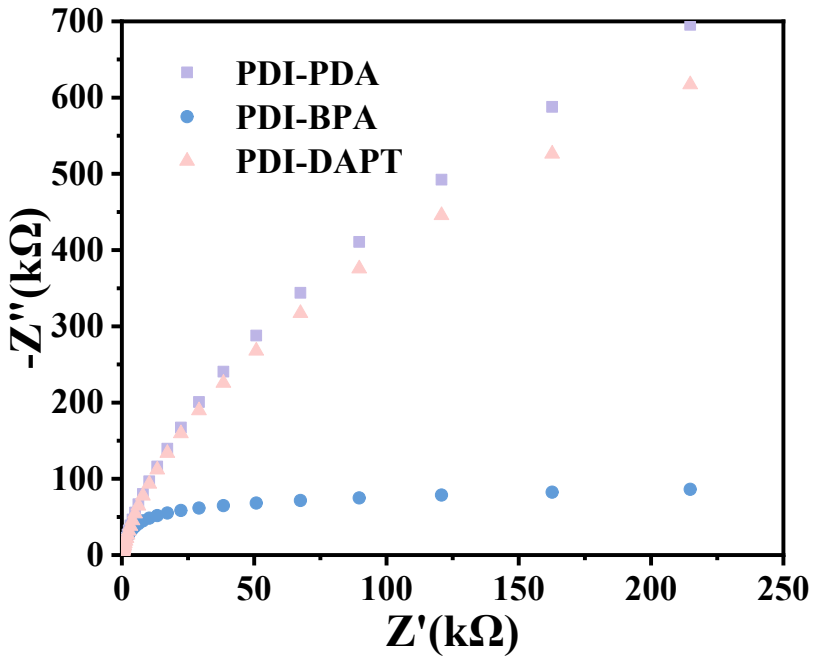

Figure S13. EIS Nyquist plots of synthesized photocatalysts

The semicircle in the low-frequency region corresponds to the charge transport resistance Rct of photogenerated-carriers. Apparently, PDI-BPA possesses a smaller Rct than PDI-PDA and PDI-DAPT in the EIS spectra (**Figure S13**), indicating it has a lower charge-transfer resistance which ensures the faster electron transfer.

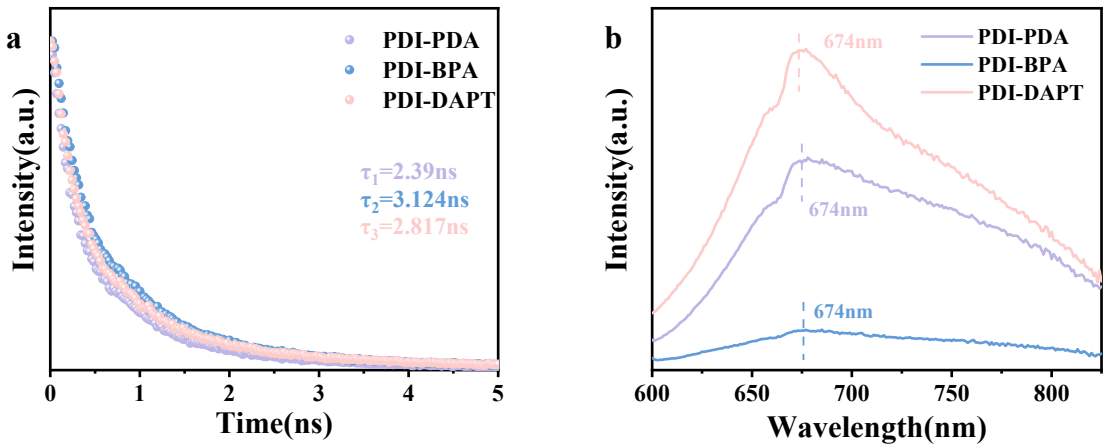

Figure S14. (a) Time-resolved PL spectra of synthesized photocatalysts; (b) Steady-state PL spectra of synthesized photocatalysts.

Compared with PDI-PDA and PDI-BPA, PDI-DAPT exhibited the shortest average fluorescence lifetime (τ) in time-resolved fluorescence spectra. Average fluorescence lifetime τ in **Figure S14** is calculate through **Equation 5**[6]

$$\tau = \frac{\sum(A_i\% \times \tau_i^2)}{\sum(A_i\% \times \tau_i)} \quad (3)$$

Where, A_i is the amplitude corresponding to each component, τ_i is the time coefficient, and the measurement data and calculation results are shown in **Figure S28**.

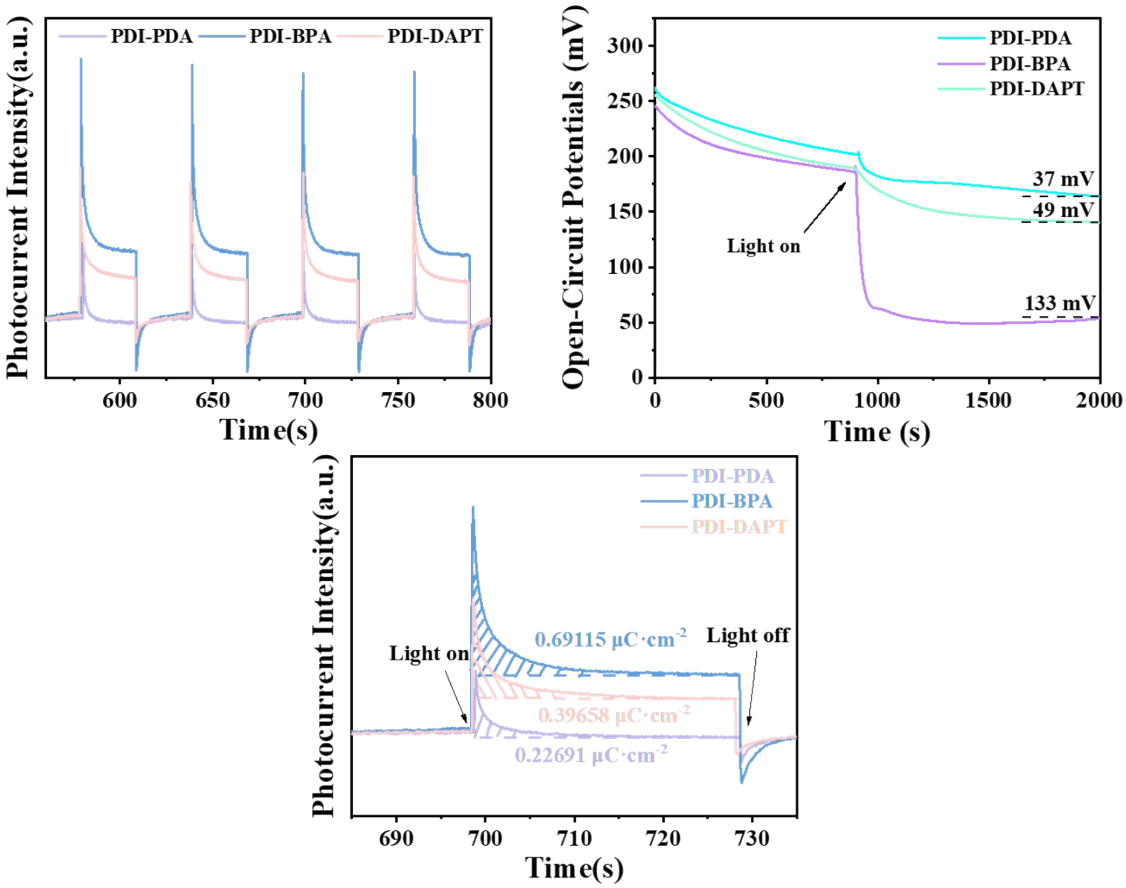

Figure S15. (a) Photocurrent-time response diagram, (b) Open circuit voltage (OCP), (c) Transient photocurrent density of PDI-PDA, PDI-BPA and PDI-DAPT.

Figure S15b presents the OCP measurement outcomes for PDI-PDA, PDI-BPA and PDI-DAPT. The high BEF value allows PDI-BPA to exhibit the highest OCP (133 mV), which is 2.7 times that of BAT (49 mV) and 3.6 times that of BAP (37 mV), respectively.

Integrate the peak and steady-state values of transient photocurrent density for PDI-PDA, PDI-BPA and PDI-DAPT during illumination with time, and subtract them to obtain the corresponding surface charge density. The results are presented in **Figure S15c**. The surface charge density of PDI-BPA (0.691 μC • cm^{-2}) is 2.5 times that of PDI-PDA (0.397 μC • cm^{-2}) and 8.9 times that of PDI-DAPT (0.227 μC • cm^{-2}), respectively.

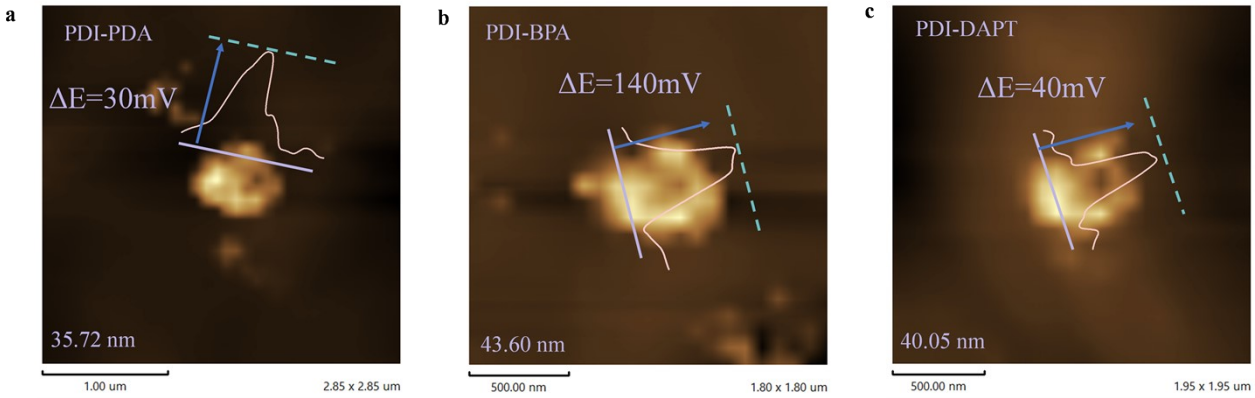

Figure S16. Surface potential maps of the three LCPs, as characterized by Kelvin probe force microscopy (KPFM)

The charge densities of CTTP and THPT were evaluated by an atomic force microscope equipped with a Kelvin probe. The surficial electrostatic potential of CTTP (280 mV) is triple the values of THPT (91mV), indicating the significantly improved internal electric field[7].

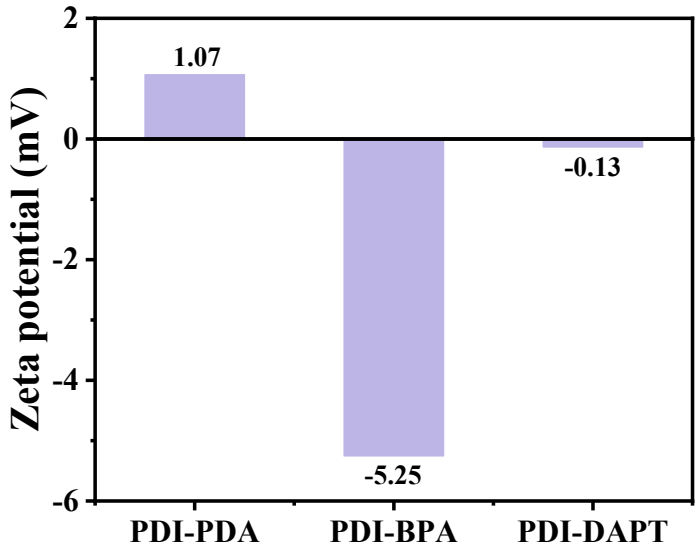

Figure S17. Zeta potential of PDI-PDA, PDI-BPA and PDI-DAPT.

Figure S17 indicates that the Zeta potential of PDI-BPA is significantly higher than that of PDI-PDA and PDI-DAPT, which evidences that PDI-BPA has the maximum surface charge density, a powerful argument for the strength of its BEF.

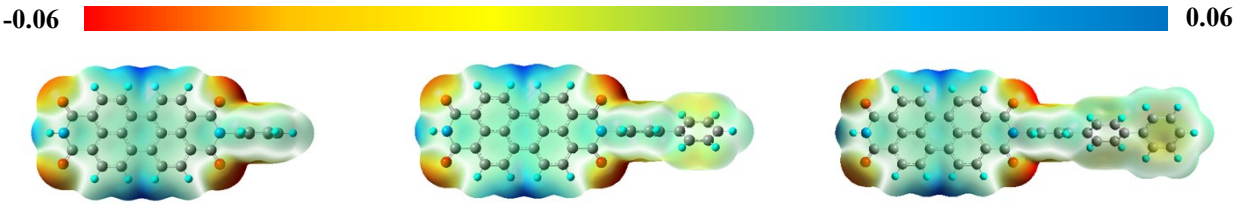

Figure S18. The ESP surface maps for optimized structures of PDI-PDA, PDI-BPA and PDI-DAPT.

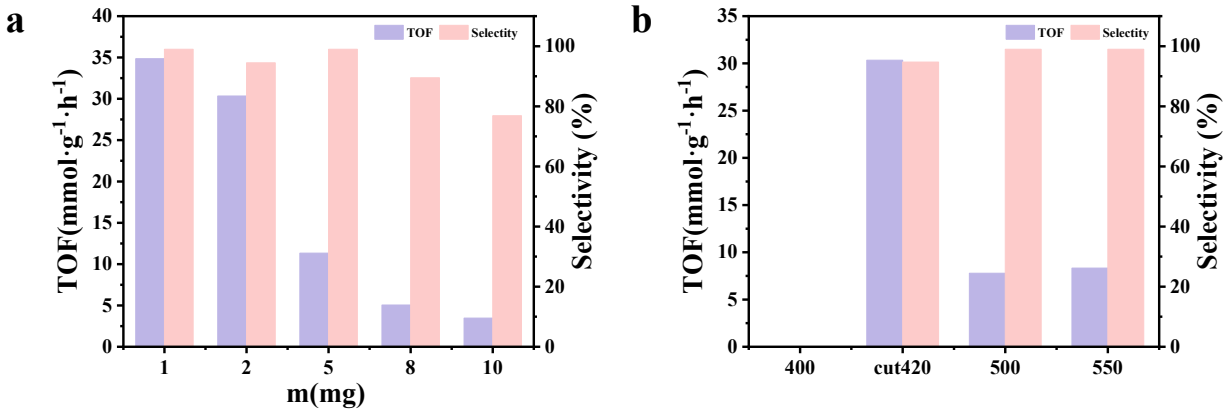

Figure S19. Comparison of the rates of PDI-BPA photocatalytic production of H_2O_2 and oxidation of benzylamine under different catalyst qualities (**Figure S20a**) and wavelengths (**Figure S21b**).

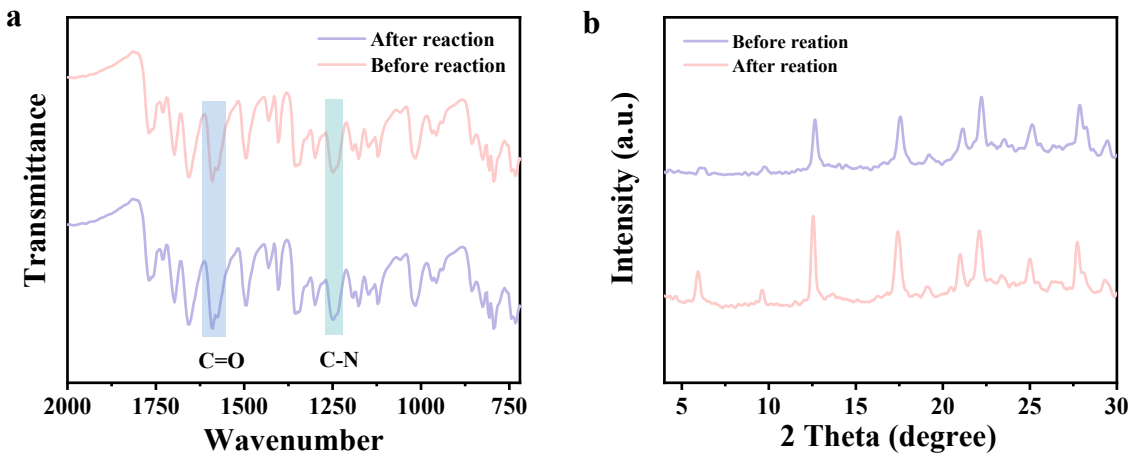

Figure S20. (a)Transmission infrared spectra for as-synthesized PDI-BPA after photocatalytic reaction; (b) XRD for as-synthesized PDI-BPA after photocatalytic reaction.

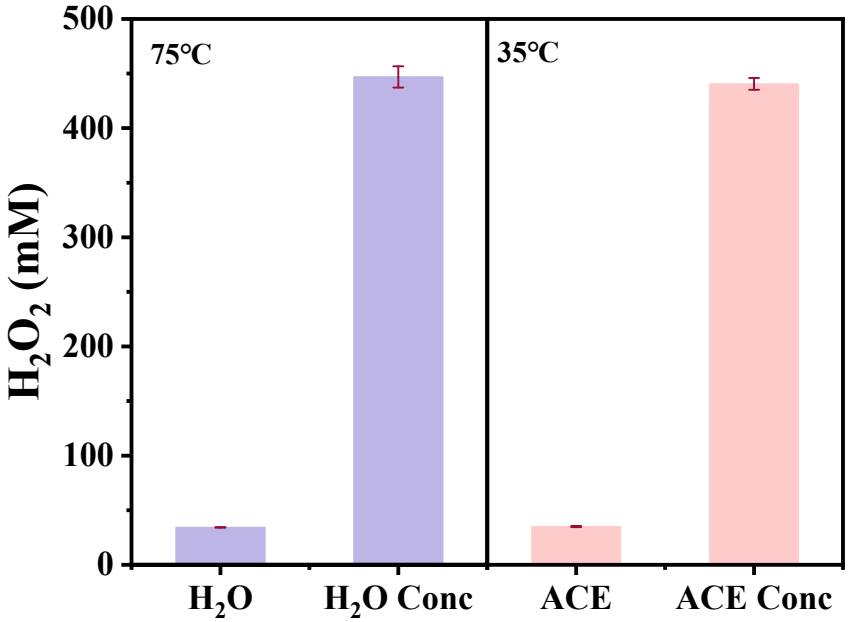

Figure S22. Comparison of temperature during vacuum distillation of H_2O and acetonitrile and the concentration of H_2O_2 after distillation.

This study compared the temperature profiles observed during the vacuum distillation of both water and acetonitrile, along with the resulting hydrogen peroxide (H_2O_2) concentrations post-distillation. The objective was to evaluate the thermal stability of H_2O_2 under reduced pressure conditions and to assess the potential for decomposition or loss during the distillation process. Results indicate that acetonitrile distilled at a lower temperature compared to water, consistent with its lower boiling point under vacuum. Furthermore, the concentration of H_2O_2 remained largely unchanged following the distillation of water, whereas a noticeable decrease was observed after distilling acetonitrile. These findings suggest that the choice of solvent influences the stability of H_2O_2 during vacuum distillation, likely due to differences in thermal energy transfer and solvent–solute interactions.

Figure S23. Comparison of total carbon (TC) content in the liquid after distillation-extraction (this work) and that obtained using ethanol as the sacrificial agent.

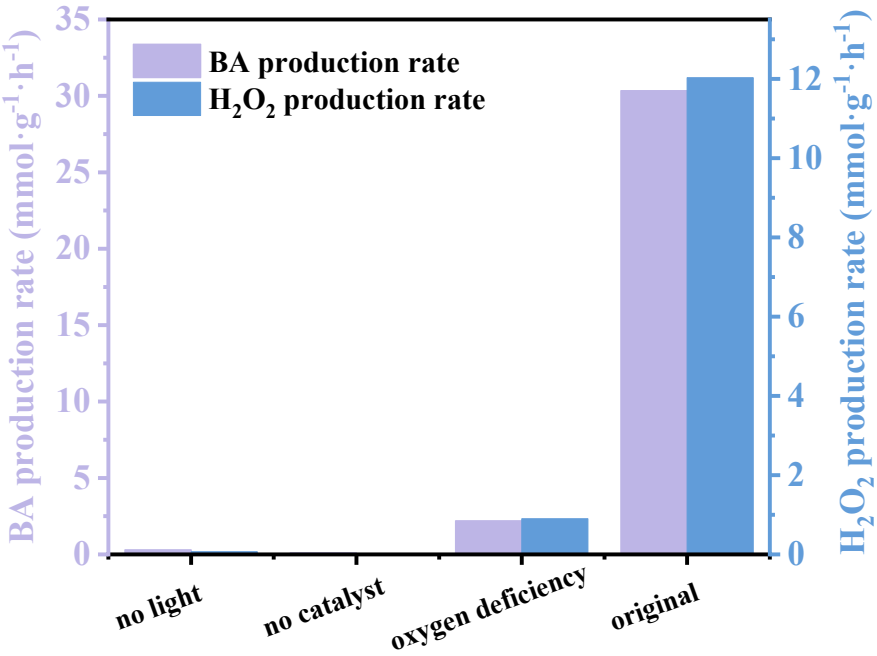

Figure S24 Comparison of the production efficiency of BA and H_2O_2 via PDI-BPA photocatalysis under conditions of no light, no catalyst, and oxygen deficiency.

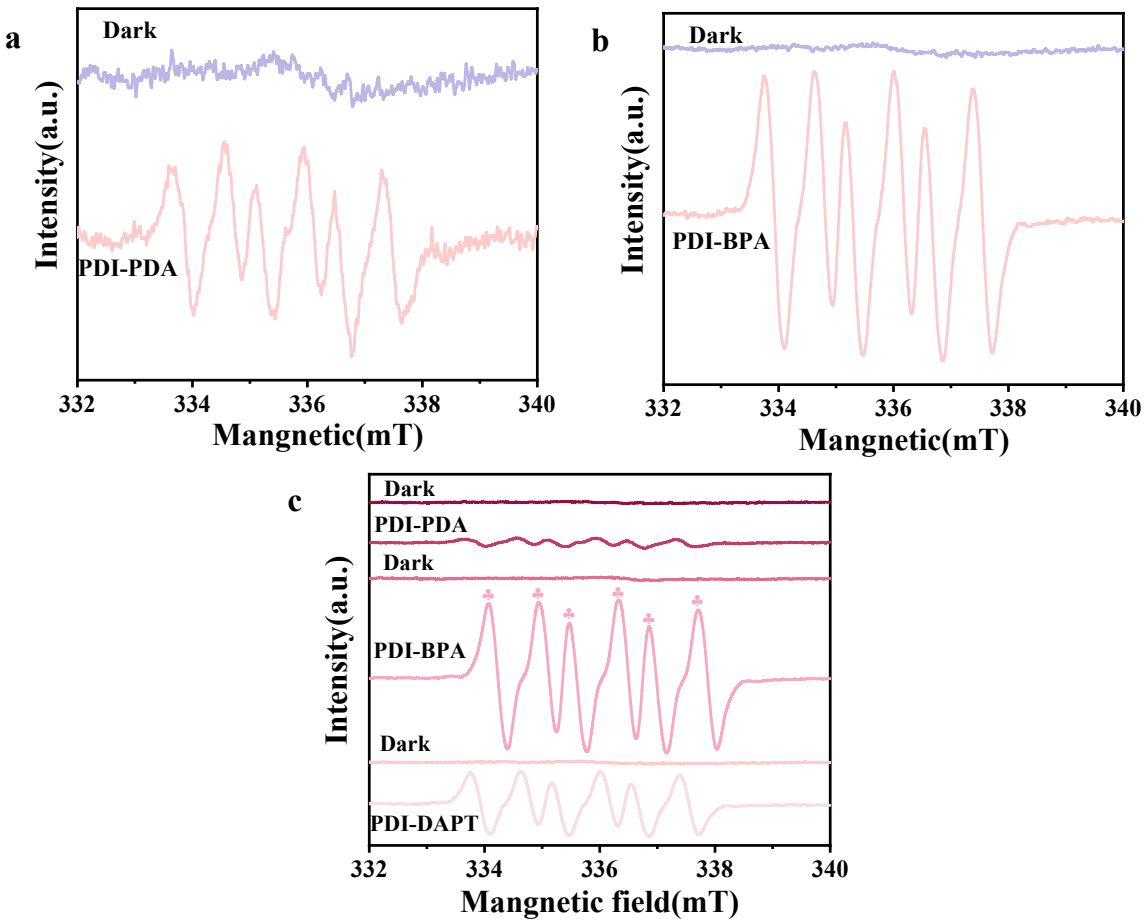

Figure S24. Superoxide radical ($\cdot O_2^-$) EPR spectra (the trapping agent is 5, 5-dimethyl-1-pyrrolin-n-oxide, DMPO) of PDI-BPA (a) and PDI-DAPT (b); (c) The comparison diagram of the EPR spectra of superoxide free radicals ($\cdot O_2^-$) within 5 minutes under three catalyst systems.

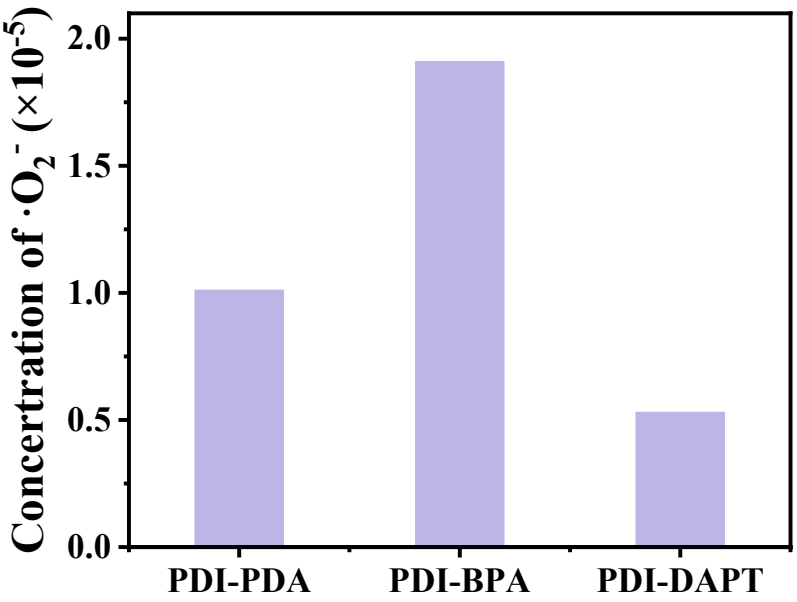

Figure S25. Photocatalytic generation of superoxide radicals (• O_2^-) for PDI-PDA, PDI-BPA, and PDI-DAPT, as measured by the nitro tetrazolium blue (NBT) method.

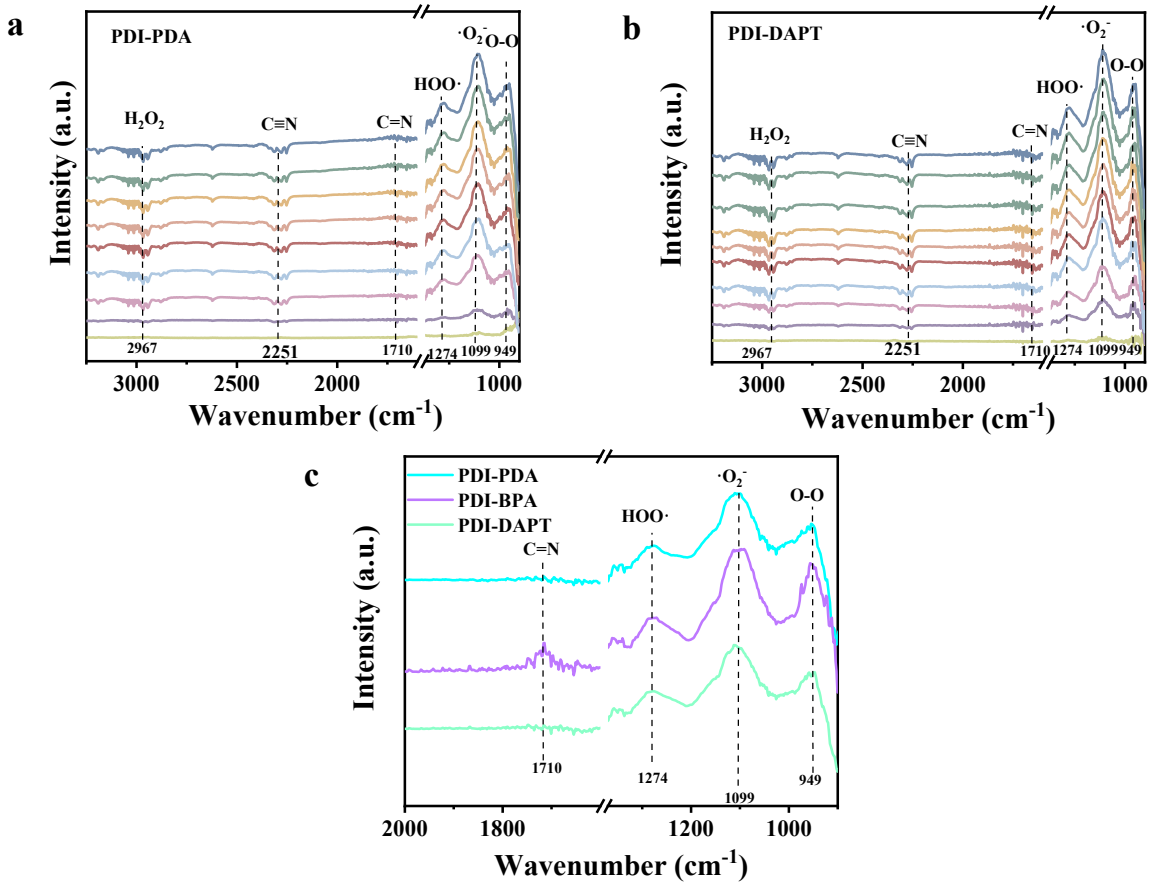

Figure S26. In situ FT-IR spectra versus illumination time for the photocatalytic system of PDI-PDA (a) and PDI-DAPT (b) in O_2 atmosphere; (c) The comparison diagram of the in situ Fourier transform infrared spectroscopy changes within 60 minutes under three catalyst systems

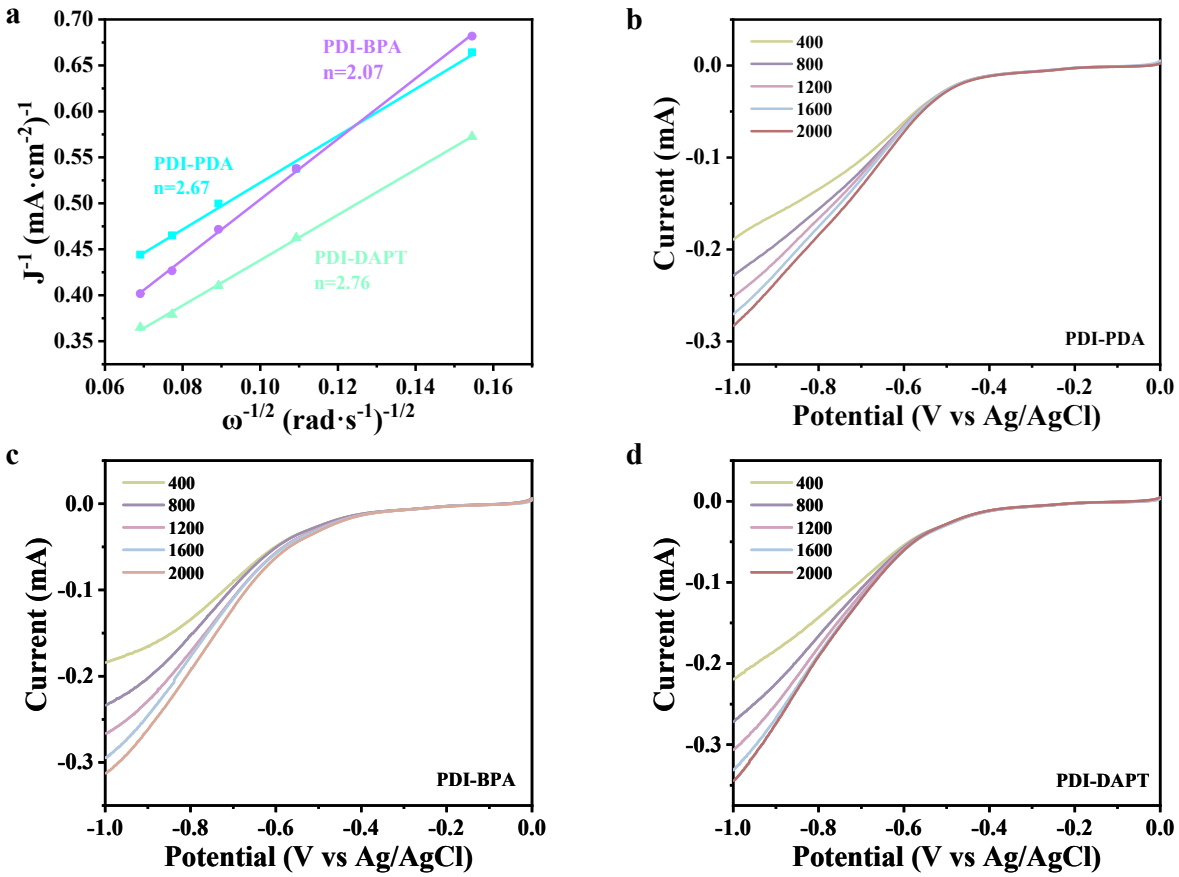

Figure S27. (a) Koutecky-Levich diagram of PDI-PDA, PDI-BPA and PDI-DAPT; Linear-sweep rotational ring disk electrode (RRDE) voltammogram for PDI-PDA (b), PDI-BPA (c) and PDI-DAPT (d).

In order to ascertain the electron transfer number during the production of H_2O_2, the reduction current of O_2 at the disk electrode and the oxidation current of H_2O at the ring electrode were measured using a rotating ring-disk electrode (RRDE). The three photocatalysts all conform to the $2e^-$ transfer process in the reaction. Compared with PDI-PDA, PDI-BPA and PDI-DAPT exhibits a tighter $2e^-$ reduction reaction, which indicates that the selectivity of H_2O_2 generation is higher. The detailed process of measuring the rotating ring disk electrode (RRDE) refers to the literature methods [8, 9]. In brief, using a glassy carbon electrode as the working electrode, a Pt ring as the counter electrode, and an Ag/AgCl electrode as the reference electrode, the ring potential of the disc-shaped electrode was maintained at 0.6 V (vs. Ag/AgCl). Then, linear sweep voltammetry (LSV) was performed in an O_2 saturated phosphate buffer solution (0.1 M, pH=7) at a scanning speed of 5 mV/s and rotation rates of 400, 800, 1200, 1600 and 2000 rpm.

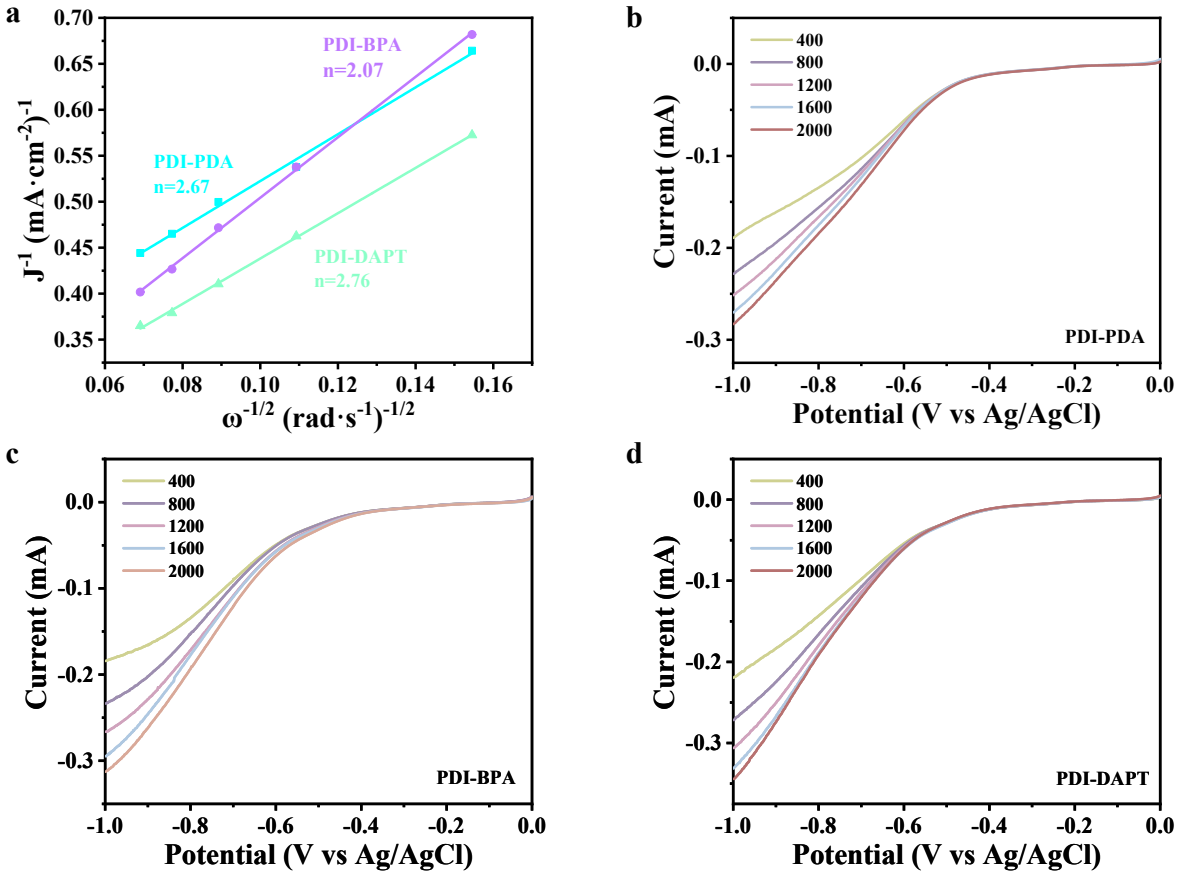

Figure S28 requires setting the ring current to -0.95V and maintaining a constant scanning rate and N_2 atmosphere. Calculate the number of transferred electrons (n) using **Equation 6**:

$$n = 4\frac{I_d}{I_d + I_r/N} \tag{4}$$

Where I_d and I_r represent the current of the disk and ring, respectively. N is the collection efficiency of RRDE, with an average value of 0.37.

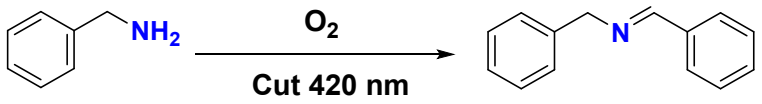

Catalyst	Solvent	Atmosphere	Reaction	Select.(%)	TOF ($\mu mol \cdot g^{-1} \cdot h^{-1}$)	Ref.
SnS_2/PPy	DMF	Air	300 W Xe lamp	99.7%	823	[10]
HNU-64	CH_3OH	O_2	$\lambda \geq 400$ nm	99	3994	[11]
Pd/BiOCl	ACN	Air	$\lambda \geq 400$ nm	99	~1666	[12]
Au@DUT-67(Zr)	DMF	O_2	,$\lambda \geq 400$ nm	~99	~1133	[13]
Py-Bde-COF	ACN	Air	white LED	~99	~1666	[14]
BiOCl/TiO_2	solvent-free	LED 10 W	λ = 400–405 nm	99	6316	[15]
NiFe2O4/rGO/Bi2WO6	DMF	Air	420 W metal halide lamp	96 %	3333	[16]
CWOH-1	ACN	N_2	λ > 420 nm	98	833	[17]
2-TTCS	ACN	Air	10 W LED white light	97.60	10000	[18]
Mn_2Ti-CPCDC	ACN	Air	10 W blue-light irradiation	99	3000	[19]
PDI-BPA	ACN	O_2	cut420nm	99	30340	This work

Table S1. Comparison of herein reported BA oxidation to N-BA results with other photocatalysts.

Table S2. Comparison of performance of photocatalysts reported in recent years for photosynthesis of H_2O_2

Catalyst	Solvent	Reaction	TOF ($\mu mol \cdot g^{-1} \cdot h^{-1}$)	Ref.
Pt/CP	H_2O	300 W Xe lamp	802	[20]
MIL-125-PDI	1mLH_2O+4mL CH_3CN	$\lambda > 420$ nm	4800	[21]
TTF-BPY-HOF	H_2O	$\lambda > 420$ nm	681.2	[22]
Hf-PMOF/APF	DMF	O_2, $\lambda \geq 400$ nm	2995.13	[23]
EFB-MOF	H_2O	$\lambda > 420$ nm	1676	[24]
Re10-MFM-67	H_2O	$\lambda > 400$ nm	8500	[25]
O-PTAQ	H_2O	100 $mW \cdot cm^{-2}$	4989	[26]
NQ-COFS1-O	ACN	N_2, $\lambda > 420$ nm	6070	[27]
CN-COF	H_2O	$\lambda > 400$ nm	6024	[28]
TA-DHPZ	H_2O	$\lambda > 420$ nm	7787	[29]
PDI-BPA	ACN	O_2, cut 420nm	10058	This work

3 References

1. X. J. Wu, B. C. Hu, D. Li, B. Y. Chen, Y. Y. Huang, Z. K. Xie, L. H. Li, N. J. Shen, F. C. Yang, W. D. Shi, M. Chen and Y. F. Zhu, *Angew. Chem. Int. Ed.*, 2023, **62**.
2. J. Chen, W. Lin, J. Lin and Y. Wang, *J. Mater. Chem. A*, 2025, **13**, 1095-1101.
3. L. Gao, H. Chai, H. Niu, J. Jin and J. Ma, *Small*, 2023, **19**, 2302665.
4. X. Wu, B. Hu, D. Li, B. Chen, Y. Huang, Z. Xie, L. Li, N. Shen, F. Yang, W. Shi, M. Chen and Y. Zhu, *Angewandte Chem. Int. Ed.*, 2023, **62**, e202313787.
5. K. Liu, J. Li, H. Qi, M. Hambsch, J. Rawle, A. R. Vázquez, A. S. Nia, A. Pashkin, H. Schneider, M. Polozij, T. Heine, M. Helm, S. C. B. Mannsfeld, U. Kaiser, R. Dong and X. Feng, *Angew. Chem. Int. Ed.*, 2021, **60**, 13859-13864.
6. L. Chen, L. Wang, Y. Wan, Y. Zhang, Z. Qi, X. Wu and H. Xu, *Adv. Mater.*, 2020, **32**, 1904433.
7. J. Xu, W. Li, W. Liu, J. Jing, K. Zhang, L. Liu, J. Yang, E. Zhu, J. Li and Y. Zhu, *Angew. Chem. Int. Ed.*, 2022, **61**, e202212243.
8. Y. Liu, W.-K. Han, W. Chi, Y. Mao, Y. Jiang, X. Yan and Z.-G. Gu, *Appl. Catal. B Enviorn.*, 2023, **331**, 122691.
9. M. Sun, X. Wang, Y. Li, H. Pan, M. Murugananthan, Y. Han, J. Wu, M. Zhang, Y. Zhang and Z. Kang, *ACS Catal.*, 2022, **12**, 2138-2149.
10. Z. Su, B. Zhang, X. Cheng, M. Xu, G. Chen, Y. Sha, Y. Wang, J. Hu, R. Duan and J. Zhang, *Dalton Trans.*, 2022, **51**, 13601-13605.
11. G. Che, W. Yang, C. Wang, M. Li, X. Li and Q. Pan, *Inorg. Chem.*, 2022, **61**, 12301-12307.
12. S. Wei, H. Zhong, H. Wang, Y. Song, C. Jia, M. Anpo and L. Wu, *Appl. Catal. B Enviorn.*, 2022, **305**, 121032.
13. C. Liu, Y. Liu, Y. Shi, Z. Wang, W. Guo, J. Bi and L. Wu, *J. Colloid Interface Sci.*, 2023, **631**, 154-163.
14. Y. Su, B. Li, H. Xu, C. Lu, S. Wang, B. Chen, Z. Wang, W. Wang, K.-i. Otake, S. Kitagawa, L. Huang and C. Gu, *J. Am. Chem. Soc.*, 2022, **144**, 18218-18222.
15. T. Zhang, W. Wang, M. He, H. Wang, Z. He, Y. Yang, K. Wang and Z. Liu, *Sep. Purif. Technol.*, 2025, **356**, 130021.
16. H. Xi, H. Wang, D. Liu, Q. Mu, X. Xu, Q. Kang, Y. Yang, Z. Yang and Z. Lei, *J. Alloys Compd.*, 2025, **1010**, 177818.
17. Z. Yue, Y. Yu, T. Hu, Y. Wang, L. Cao, Y. Zhang, Y. Chang, L. Pei and J. Jia, *Mater. Today Chem.*, 2024, **36**, 101932.
18. Y. Ge, Y. Hu, X. Ma, Y. Chen, J. He, L. Jiang, Z. Yan and J. Wang, *ACS Appl. Nano Mater.*, 2024, **7**, 1233-1244.
19. X. Zhang, X. Pan, X. Si, L. Zhu, Q. Yao, W. Duan, X. Huang and J. Su, *Inorg. Chem.*, 2024, **63**, 19408-19417.
20. R. Zhang, H. Xu, Z. Huang, J. Zhang, L. Liu, Z. Ma, Z. Zhang, K. Wang, P. Liu, H. Liu and X. Zheng, *Adv. Funct. Mater.*, 2025, **35**, 2420504.
21. X. Chen, Y. Kondo, S. Li, Y. Kuwahara, K. Mori, D. Zhang, C. Louis and H. Yamashita, *J. Mater. Chem. A*, 2021, **9**, 26371-26380.
22. J. Zhang, Z. Ge, J. Wang, D. Zhong and T. Lu, *Nat. Commun.*, 2025, **16**, 2448.
23. H. He, Z. Wang, J. Zhang, S. Mamatkulov, O. Ruzimuradov, K. Dai, J. Low and Y. Li, *Energy Environ. Sci*, 2025, **18**, 6191-6201.
24. J. Y. Choi, B. Check, X. Fang, S. Blum, H. T. B. Pham, K. Tayman and J. Park, *J. Am. Chem. Soc.*, 2024, **146**, 11319-11327.

25. B. Tang, D. Brooks, M. He, Y. Chen, Z. Hu, X. Han, J. Li, S. Zhou, J. Fan, Y. Ye, I. da Silva, C. Li, Z. Wang, L. Shan, B. Han, W. Li, D. Polyukhov, B. An, C. Dejoie, M. Wilding, S. Xu, M. Kippax-Jones, Z. Zhu, Y. Ma, F. Tuna, E. J. L. McInnes, S. J. Day, S. P. Thompson, M. D. Frogley, L. S. Natrajan, M. Schröder and S. Yang, *J. Am. Chem. Soc.*, 2025, **147**, 24326-24335.
26. P. Jiang, Y. Huang, X. Jiang, H. Yan, S. Liu, Z. Chen, X. Wu, X. Zhou, Y. Ye and G. Ouyang, *Adv. Sci.*, 2025, **12**, e03929.
27. H. Pang, M. Tan, T. Guo, Z. Zhang, Y. Zhu, C. Ding, M. Wang, Y. Xiang and D. Huang, *J. Mater. Chem. A*, 2025, **13**, 9274-9281.
28. Z. Yu, F. Yu, M. Xu, S. Feng, J. Qiu and J. Hua, *Adv. Sci.*, 2025, **12**, 2415194.
29. J. Zhang, L. Tian, S. Feng, Z. Wang, W. Yu, K. Hu and J. Hua, *Chem. Eng. J.*, 2025, **506**, 160024.